

pubs.acs.org/JPCC Article

# Type II Germanium Clathrates from Zintl Phase Precursor Na<sub>4</sub>Ge<sub>4</sub>: Understanding Desodiation Processes and Sodium Migration Using First-Principles Calculations

Anirudh Nandakumar, Xihong Peng,\* and Candace K. Chan\*



Cite This: https://doi.org/10.1021/acs.jpcc.3c02343



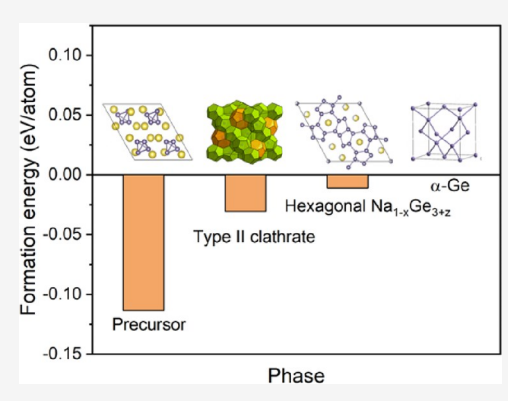
ACCESS I

Metrics & More

Article Recommendations

Supporting Information

ABSTRACT: Type II germanium clathrates have recently been investigated for potential applications as anodes in batteries due to their cage-like structures that can accommodate electrochemical insertion of guest ions. To synthesize type II Ge clathrates (Ge $_{136}$ ), several experimental routes use thermal or electrochemical desodiation of the Zintl phase compound Na $_4$ Ge $_4$ . However, the mechanism by which Na atoms are removed from the precursor to form clathrates is not well understood. Herein, we use first-principles density functional theory and nudged elastic band calculations to understand the reaction mechanism and formation energies of the products typically observed in the synthesis, namely, Na  $_{\delta}$ Ge $_{136}$  (0 <  $\delta$  < 24) type II clathrates and hexagonal phase Na $_{1-x}$ Ge $_{3+z}$ . Specifically, we confirm the energetic feasibility of Na vacancy formation in Na $_4$ Ge $_4$  and find that the barrier for Na vacancy migration is only 0.37 eV. This relatively low energy barrier is consistent with the ease with which Na  $_4$ Ge $_4$ can be desodiated to form the products. We also discuss the energetics, sodium migration pathways, and



potential electrochemical performance of Ge<sub>136</sub> as anode material for Na-ion batteries. Overall, this study highlights how first-principles calculations can be used to understand the synthesis mechanism and desodiation processes in clathrate materials and will help guide researchers in the design and evaluation of new open framework compounds as viable materials for energy storage applications.

#### 1. INTRODUCTION

Tetrel clathrates are a class of host–guest crystalline structures that exhibit interesting characteristics such as superconductivity, agnetism, hydrogen storage, tunable optical properties, hydrogen storage, tunable optical properties is the unique interactions between the host framework and guest atoms, as well as the defects associated with this structural type. For example, consider the type II clathrate with the general formula M of the structural type. Where M are alkali or alkaline earth metals (e.g., Na, K, Ba) and Tt are Tetrel elements (e.g., Si, Ge, Sn). Deviation from this stoichiometry can take place in the form of guest atom vacancies or framework substitutions, which can result in a wide structural landscape with great potential for controlling and tuning the material properties of the clathrates. 11,13,14

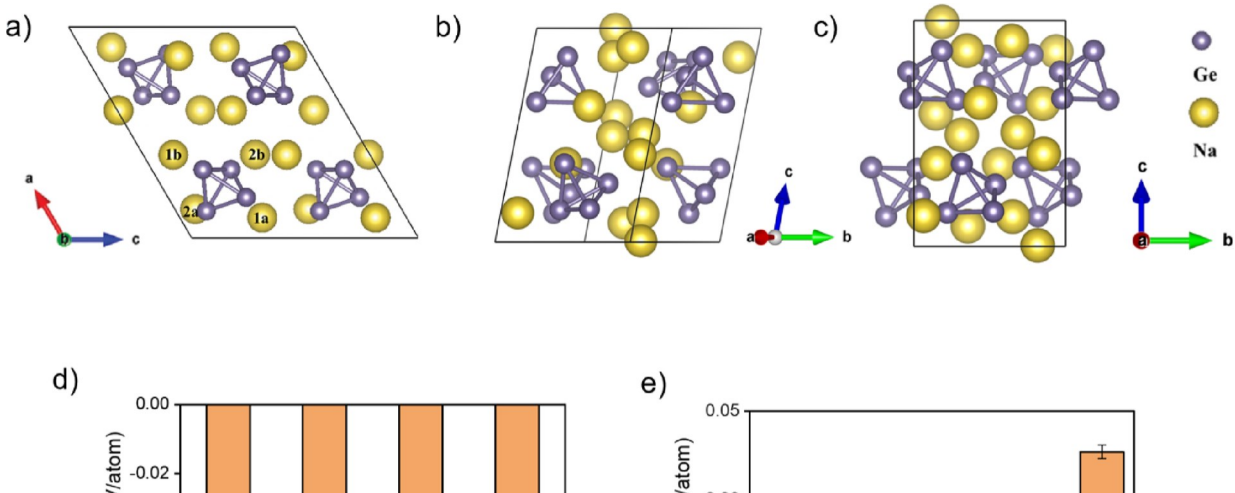
Recently, there has been much interest in the electrochemical properties of clathrates and their potential for applications in batteries. 5-7,15,16 Our group has extensively investigated the possibility of using Si, Ge, and Sn clathrates as potential anodes for Li and Na-ion batteries. 17-23 In addition to the experimental studies, we also carried out *ab initio* density functional theory (DFT) studies to understand the preferred Li (Na) sites in the structures as well as the Li (Na) migration mechanisms, 22,24,25 with certain clathrate structures displaying

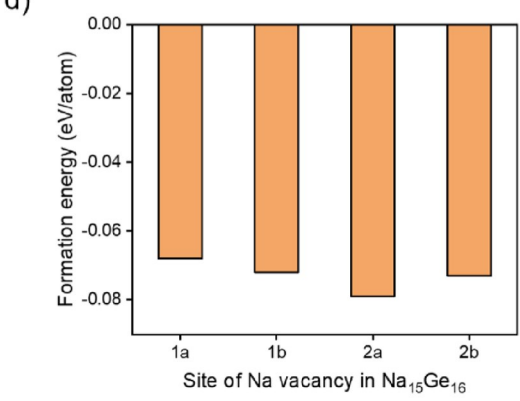
energy barriers for Li migration on the order of 0.4 eV or lower,<sup>25</sup> making them promising materials for Li-ion battery applications. The DFT studies have also provided new insights into battery material selection by elucidating the formation energy, electronic structure, open circuit voltage, and the guest atom diffusion paths in the lithiated (sodiated) phases.<sup>26–29</sup>

Understanding the mobility of guest atoms within clathrate structures is important not only for battery applications but also because the synthesis of some clathrates relies on the removal of these metals via thermal evaporation  $^{30-32}$  or oxidative deintercalation.  $^{8,33-41}$  Our research group's recently reported method  $^{36}$  for synthesizing type II germanium clathrate (Na  $_{24-\delta} \text{Ge}_{136}$ ) via solid-state electrochemical oxidation of the Zintl phase compound Na  $_4\text{Ge}_4$  showed that the products were temperature dependent, with the type II Ge clathrate forming at a relatively low temperature (300 °C), hexagonal Na  $_{1-x}\text{Ge}_{3+z}$  at intermediate temperature (350 °C),

Received: April 7, 2023 Revised: June 7, 2023







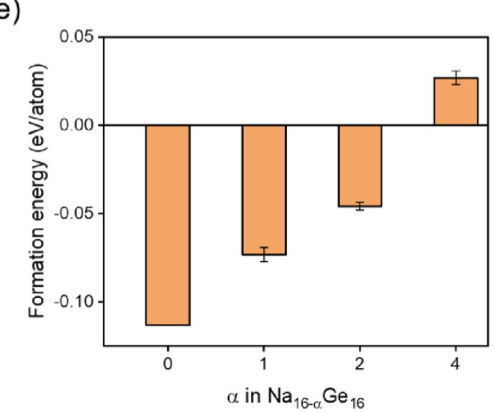


Figure 1. (a) Crystal structure of the Zintl phase precursor Na  $_4$ Ge  $_4$  (Na  $_{16}$ Ge  $_{16}$ ) viewed along the b-axis with the nonequivalent 1a, 1b, 2a, and 2b Na sites. (b, c) Additional views of the 3-dimenstional crystal structure of the Zintl phase precursor. (d) Calculated formation energies for Na  $_1$ Ge with the vacancy at each of the four different Na sites. (e) Formation energy versus Na content in Na  $_{16-\alpha}$ Ge $_{16}$ , where  $\alpha$  represents the number of Na atoms removed from the unit cell. The reported formation energy for  $\alpha$  = 1 is the average of the calculated values for the Na vacancy at each of the four different sites calculated configurations. Similarly, the average formation energies are shown for  $\alpha$  = 2 or 4 (two configurations each, see text for more details).

and diamond cubic  $\alpha$ -Ge at higher temperature (400 °C). However, to the best of our knowledge, none of the previous studies focused on understanding the mechanism of the precursor oxidation, and little attention has been paid to understanding how Na atoms are removed from the precursor that is used to synthesize the clathrates.

Herein, for the first time, we use DFT and nudged elastic band (NEB) calculations to understand the energetics and resulting mechanism of Na vacancy diffusion through the Zintl phase precursor and the products that are synthesized from it. Specifically, we confirm the energetic feasibility of Na vacancy formation in the precursor and find that the barrier for Na vacancy migration in Na<sub>4</sub>Ge<sub>4</sub> is only 0.37 eV. This relatively low barrier is consistent with the ease with which the compound can be desodiated to form the products. We also carried out a computational investigation of the three different products observed experimentally<sup>36</sup> in the electrochemical oxidation of the precursor, and we assess the potential electrochemical performance of the type II Ge clathrate as anode material for Na-ion batteries. To this end, the voltage and volume changes upon sodium intercalation (deintercalation) were calculated and the sodium mobility within the open-cage network of Ge<sub>136</sub> was investigated. The insights from this study will help guide researchers in the design and experimentation of novel synthetic methods for these open framework materials.

#### 2. COMPUTATIONAL METHODS

First-principles DFT calculations were performed using a similar manner as in our previous works.  $^{22,24}$  The calculations were carried out using the VASP code,  $^{42,43}$  the PBE functional,  $^{44}$  and projector augmented wave (PAW) potentials with a plane wave basis set.  $^{43}$  In the PAW potentials, the Ge 3d, 4s, 4p, and Na 3s, 2p electrons were treated as valence electrons. The kinetic energy cutoff for the plane wave basis set was chosen to be 400 eV, and the reciprocal space was sampled with the Monkhorst-Pack meshes  $3 \times 3 \times 3$  centered at  $\Gamma$ . The convergence criteria for the electronic and ionic relaxations were set to be 0.01 and 0.1 meV, respectively.

The formation energies for all structures were obtained using the equations described in our previous work.<sup>22,24</sup> The generalized formula can be written as shown in eq 1:

$$E_{\text{form}} = \frac{E(\text{Na}_{\beta}\text{Ge}_{\gamma}) - \beta E(\text{Na}) - \gamma E(\text{Ge})}{\beta + \gamma}$$
(1)

where  $E(\mathrm{Na_{8}Ge_{\gamma}})$  refers to the total energy of the structure  $\mathrm{Na_{8}Ge_{\gamma}}$  obtained from the DFT calculations,  $E(\mathrm{Na})$  and  $E(\mathrm{Ge})$  are the elemental energies for body-centered cubic Na and diamond cubic Ge (-1.311 and -4.621 eV/atom, respectively), and  $E_{\mathrm{form}}$  is the formation energy of the structure per atom (eV/atom). Eq 2 shows example calculations for the formation energy of Na-filled type II clathrate,  $\mathrm{Na_{24}Ge_{136}}$ .

$$E_{\text{form}} = \frac{E(\text{Na}_{24}\text{Ge}_{136}) - 24E(\text{Na}) - 136E(\text{Ge})}{160}$$
 (2)

The Gibbs free energy change of reaction ( $\Delta G_{\rm p}$ ) and the average voltage for Na removal from the Na-filled type II clathrate structure for Na compositions between  $\delta_1$  and  $\delta_2$  (with  $\delta_1 > \delta_2$ ) were calculated using eqs 3 and 4, respectively:

$$\Delta G_{\rm r} = E({\rm Na}_{\delta_1} {\rm Ge}_{136}) + (\delta_1 - \delta_2) E({\rm Na}) - E({\rm Na}_{\delta_1} {\rm Ge}_{136})$$
(3)

$$V(\delta) = -\frac{\Delta G_{\rm r}}{\delta_1 - \delta_2} \tag{4}$$

with the Na removal reactions being of the form shown in eq 5:

$$Na_{\delta_1}Ge_{136} \rightarrow Na_{\delta_2}Ge_{136} + (\delta_1 - \delta_2)Na$$
 (5)

In the standard ground-state DFT calculations at zero temperature, the Gibbs free energy change  $\Delta G_r$  ( $\equiv \Delta E_r + P\Delta V_r - T\Delta S_r$ ) can be approximated to be the change in internal energy ( $\Delta E_r$ ) at 0 K, since the terms  $P\Delta V_r$  and  $T\Delta S_r$  are order of magnitude less than  $\Delta E_r^{45}$ 

The climbing image NEB method was used to find the minimum energy paths between known reactants and products. All NEB calculations used a band with 5 or 7 intermediate images between the initial and final images. The constrained optimization of the NEB calculations was performed by adding spring forces with a spring constant 5.0 eV/Ų along the band between images, and the images were converged until the force on each image was below 0.03 eV/Å in the directions perpendicular to the band.

A slab model of the type II Ge clathrate with a (001) surface was built to simulate Na migration from within the  $Ge_{20}$  cage to outside of the clathrate structure (section 3.6.3). The slab was created with a thickness of 15.5 Å in the c-axis, and periodic boundary conditions were applied to the other two directions (a,b). The bottom half atom positions in the slab were fixed, and the top half positions were allowed to relax to mimic a surface configuration. A vacuum space beyond 18 Å was added to the simulation cell to minimize the interactions between the slab and its periodic images resulted from periodic boundary conditions.

All crystal structure figures were created with Vesta<sup>47</sup> and Diamond.<sup>48</sup> and movies with Jmol.<sup>49</sup>

#### 3. RESULTS AND DISCUSSION

**3.1. Stability of the Zintl Phase Precursor**  $Na_4Ge_4$ . Since the Ge clathrate and other byproducts are formed by sodium removal from the  $Na_4Ge_4$  precursor, we carried out DFT calculations to investigate the likely sites for creating Na vacancies as well as the formation energies of the sodium deficient compounds. The monoclinic Zintl phase compound  $Na_4Ge_4$  contains isolated homo-tetrahedranide clusters of  $[Ge_4]^{4^-}$ , each surrounded by four sodium atoms that belong to nonequivalent Na 1a, 1b, 2a, and 2b sites (Figure 1a). Because there are 4 formula units per unit cell (Z=4), making a total of 16 sodium atoms per unit cell, we refer to the stoichiometric, vacancy-free compound as  $Na_{16}Ge_{16}$  in the following discussion. Our calculated lattice parameters for this compound are in good agreement with those reported experimentally, and a comparison between the two is provided in Table S1.

The formation energy for creating a vacancy at all possible Na sites was calculated to identify the site(s) most likely to be desodiated during thermal or electrochemical oxidation of

 $Na_{16}Ge_{16}$  The calculated formation energies in Figure 1d were negative for a single vacancy at each site, indicating that it is energetically favorable to form  $Na_{15}Ge_{16}$  or the Zintl phase precursor with 6.25% Na vacancy density (1 out of 16). The lowest formation energy was observed for the Na vacancy at the 2a site; thus, the sites for creating Na vacancies were chosen by following the formation energies in Figure 1d (energy of site 2a < 2b < 1b < 1a).

Next, to consider the precursor with two Na vacancies (i.e., Na<sub>14</sub>Ge<sub>16</sub> or the precursor with 12.5% Na vacancy density), we investigated two geometrical configurations. In the first case, both vacancies were created at the 2a sites (note that there are four equivalent 2a sites in the unit cell) because of its lowest formation energy. In the second case, one Na was removed from the 2a site and the other Na atom from the 2b site. Likewise, we also considered two configurations for the precursor with four Na vacancies (i.e., Na<sub>12</sub>Ge<sub>16</sub>, or the precursor with 25% Na vacancy density). The first one is the structure with all four vacancies at the 2a sites, in the second case, two Na vacancies at the 2a sites and the remaining two at the 2b sites. The detailed site combinations and formation energy for each configuration are shown in Table S2, while Figure 1e reports the average formation energies for  $\alpha = 1, 2$ , or 4 Na vacancies in Na  $_{^{16-\alpha}}$ Ge  $_{^{16}}$ . The negative formation energies observed for  $\alpha$  = 1 and 2 suggest that the slightly Nadeficient compound is still stable. The experimental voltage profile in our experimental study<sup>36</sup> showed that the initial stages of Na<sub>16</sub>Ge<sub>16</sub> electrochemical oxidation were accompanied by a varying voltage corresponding to a single-phase process. We previously attributed this feature to the removal of excess Na from the precursor (i.e., from  $Na_{16+\alpha}Ge_{16}$ ); however, considering the above formation energies, it is also possible that this feature originates from the removal of Na from Na<sub>16</sub>Ge<sub>16</sub>. Figure 1e shows that the formation energy increases as more Na vacancies are formed, implying that it is unfavorable for a large amount of Na to be removed from the precursor. Once the Na has been removed to reach a composition of Na<sub>12</sub>Ge<sub>16</sub>, the compound is no longer stable, and there is a driving force to form other phases. This also supports our experimental findings<sup>36</sup> that, as Na is extracted from the Zintl phase precursor via controlled oxidation, it reaches a point when it becomes unfavorable to retain the structure and it hence transforms into the products (i.e., type II clathrate at 300 °C,  $Na_{1-x}Ge_{3+z}$  at 350 °C, and  $\alpha\text{-Ge}$  crystal at 400 °C) via a two-phase reaction mechanism. The calculation results for these product phases will be discussed in the next

**3.2.** Properties of Type II Ge Clathrate with Different Na Content. In our previous work, when electrochemical oxidation of Na  $_{16}$  Ge  $_{16}$  was performed at 300 °C, the product predominantly comprised type II Ge clathrates, with Rietveld analysis showing 50 wt % of nearly guest-free clathrate (refined composition of Na  $_{0.3(1)}$  Ge  $_{136}$ ), with the balance being the impurity phase, hexagonal Na  $_{1-X}$  Ge  $_{3+2}$ . A two-phase reaction mechanism was observed, with the Ge clathrate forming at the expense of the Zintl phase precursor. This is consistent with the driving force for the precursor to transform to another phase once the desodiation has destabilized the structure as discussed in the previous section.

The type II clathrate is described by the Fd-3m space group. Each unit cell contains 8  $Tt_{28}$  cages (hexakaidecahedra) and 16 smaller  $Tt_{20}$  cages (dodecahedra) shown in orange and green,

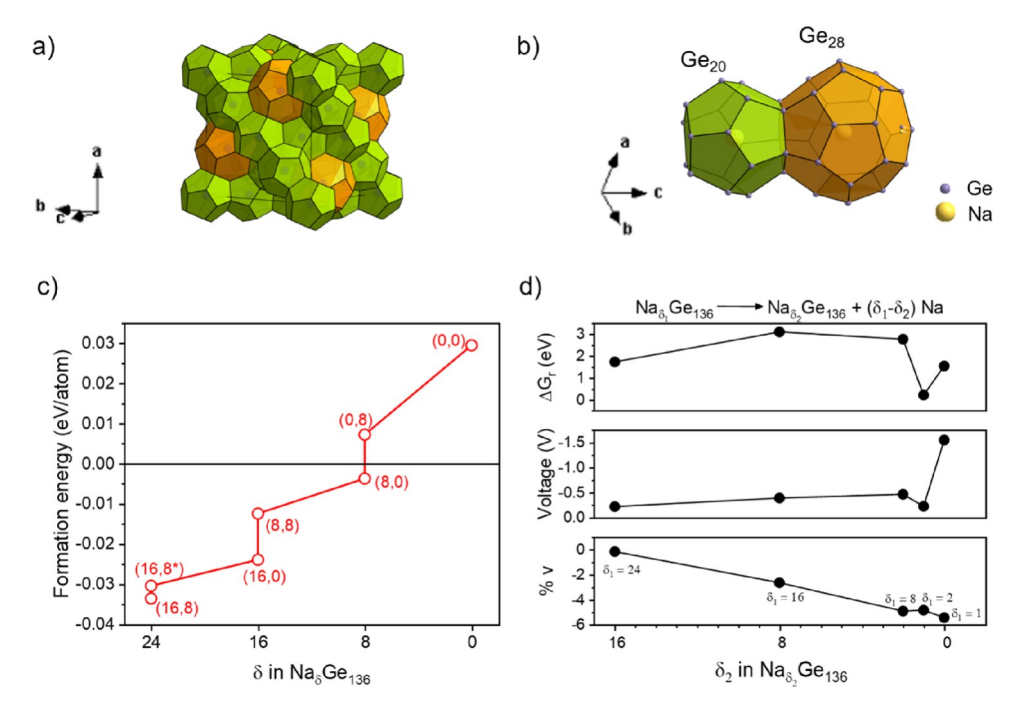


Figure 2. (a) Polyhedral model of the type II clathrate Na  $G_{13}(b)$  Schematic of the two types of polyhedra in the type II clathrate structure with Na as a guest atom in the cage centers: dodecahedra (Ge , greep) and hexakaidecahedra (Ge , orange). (c) Formation energy versus Na content ( $\delta$ ) in Na Ge  $_{36}$  where each point is identified by indices (a, b); a = number of Na atoms in the Ge  $_{26}$  cage centers, b = number of Na atoms in the Ge  $_{28}$  cage center. (d) Gibbs free energy change and corresponding potentials for the Na removal reaction for the most stable Na  $_{62}$ Ge  $_{136}$  structures. The percentage volume change (%v) upon Na removal as a function of the Na-filled clathrate i.e., Na $_{24}$ Ge $_{136}$ .

respectively, in Figure 2a,b. The Tt atoms reside at the vertices of the polyhedra (hexagonal or pentagonal faces in the Tt  $_{\rm 28}$  cages, pentagonal faces in the Tt  $_{\rm 20}$  cages), whereas the guest atoms occupy the centers of the cages.  $^{\rm 33}$ 

To better understand why both (nearly) guest-free and Nafilled Ge clathrates were observed in the synthesis, DFT calculations were performed for the Ge clathrate with varying amounts of Na content, i.e.,  $\delta$  in Na  $_{\delta}$ Ge  $_{136}$ . Our previous DFT studies<sup>21,36</sup> on type II clathrates showed that guest atoms can adopt positions in the  ${\rm Tt}_{20}$  and  ${\rm Tt}_{28}$  cage centers. Additionally, due to the large  ${\rm Tt}_{28}$  cage volume, it is energetic feasible for guest atoms to be positioned off-centered, i.e., close to a hexagonal face ("Off hex") or a pentagonal face ("Off pent"), with guest atoms in the Off hex positions of the Tt  $_{28}$  cages showing the lowest energies.  $^{21,36}$  A schematic showing Na atoms occupying the center and two off-centered positions inside a  $\operatorname{Ge}_{28}$  cage is shown in Figure S1. The formation energies for the various clathrate structures are shown in Figure 2c; the indices next to each data point indicate the number of Na atoms in the Ge<sub>20</sub> cage centers (corresponding to the first number) and in the Off hex positions of the Ge<sub>28</sub> cage (corresponding to the second number). The configuration of Na<sub>24</sub>Ge<sub>136</sub> with 8 Na atoms within Off hex positions in the  $Ge_{28}$  cages, corresponding to (16,8), had a formation energy of -0.0336 eV/atom. This is slightly lower than the formation energy of  $Na_{24}Ge_{136}$  with Na at the centers of all  $Ge_{20}$  and  $Ge_{28}$  cages, corresponding to (16,8\*), which was found to be -0.0305 eV/atom. These results again indicate that Na atoms inside the larger  $Ge_{_{2R}}$  cages prefer the Off hex position instead of the cage center, consistent with our previous findings. 21,36

In reducing the Na content to a composition of  $Na_{16}Ge_{136}$ , two configurations were considered, denoted as (8,8) and

(16,0) in Figure 2c. In the (16,0) configuration with all 16 Na atoms located at the Ge<sub>20</sub> cage centers, the formation energy was found to increase compared to Na<sub>24</sub>Ge<sub>136</sub> implying that the completely guest-filled clathrate is more stable than the clathrate with empty cages. This suggests that the presence of Na atoms in the cages helps to stabilize the structure. In the second Na  $_{16}$  Ge  $_{136}$  configuration of (8,8) (i.e., half of the Ge  $_{20}$  cage centers filled by Na and all 8 of the Ge  $_{28}$  cages filled by Na in Off hex positions), the formation energy is slightly higher than the (16,0) configuration, indicating it is energetically more favorable for Na to occupy the small Ge 20 cage over the larger Ge<sub>30</sub> cage. This suggests that Na removal from the type II Ge clathrate would preferentially take place from the Ge cages, whereas Na removal from the small cages is energetically unfavorable. This observation is consistent with Na diffusion in type II Si clathrates as well.<sup>51</sup> The preference of Na to occupy the smaller  $Ge_{20}$  cage may be due to its smaller cage volume and more symmetric cage geometry (since the Ge 20 cage is made solely of pentagonal faces as opposed to the Ge28 cage, which comprises both hexagonal and pentagonal faces) for better accommodation of Na. This result is similar to the findings in our previous calculations involving guest-free type I<sup>25</sup> and type II silicon clathrates, <sup>21</sup> wherein it was observed that Li atoms preferred to occupy the centers of the small cages.

When further reducing the Na content to a composition of  $Na_8Ge_{136}$ , two configurations were considered, denoted as (8,0) and (0,8) in Figure 2c. The formation energy of (8,0) was lower than that of (0,8), which again shows that Na prefers to occupy the small  $Ge_{20}$  cage rather than  $Ge_{28}$ . For the (0,8)  $Na_8Ge_{136}$ , structure, the formation energy was found to depend on the Na location inside the large  $Ge_{28}$  cages, following the trend: Off hex < Off pent < center (i.e., 0.0072, 0.0077, and 0.0096 eV/atom, respectively). This is also consistent with our

previous findings for  $Na_1Ge_{136}$ . Finally, the formation energy for the guest-free clathrate ( $Ge_{136}$ ) was found to be 0.0295 eV/atom

From these results, we can see that the size and geometry/ shape of the cage are important for the energetics of the Na insertion sites. It is energetically favorable to form Ge type II clathrates with high Na-content, which is in agreement with our previous study on Na-filled type II silicon clathrates, 17 wherein we noted that  $\mathrm{Na_{24}Si}_{136}$  is more stable compared to guest-free Si<sub>136</sub>. According to the results in Figure 2c, the formation energies for nearly guest-free clathrates (or low-Na content clathrates) are presumed to fall in the range of 0.01-0.03 eV/atom. The fairly low formation energies, although positive, indicate the possibility that these clathrates can be synthesized, particularly if the Na adopts the positions inside the Ge<sub>20</sub> cages. The completely guest-free clathrate (Ge 136) has the highest formation energy and therefore should be harder to synthesize than the Na-filled clathrates. Indeed, to our knowledge, most previous attempts at synthesizing guest-free type II germanium clathrates have resulted in the formation of Na-filled clathrates<sup>39,41,52</sup> or low-Na/K content clathrates<sup>30,37</sup> as one of the major products along with other by-products. Special techniques such as the application of an electric field in an Ar environment,<sup>31</sup> and chemical oxidation,<sup>53</sup> or thermal decomposition<sup>38</sup> in ionic liquid media were needed to obtain nearly guest-free type II Ge clathrates ( $\delta$  2 0 in Na Ge <sub>13</sub>).

Figure 2d presents the Gibbs free energy change of the reaction ( $\Delta G$ ) computed from eq 3 and corresponding voltage as a function of Na content computed using eq 4 for Na Ge 136  $(\delta = 16, 8, 2, 1, \text{ and } 0)$ . The positive  $\Delta G$ , values (and negative voltages) indicate that desodiation of Na<sub>24</sub>Ge<sub>136</sub> requires external biasing, while the reverse reaction (i.e., sodiation of empty  $Ge_{136}$  to form  $Na_{\delta}Ge_{136}$ ) would be spontaneous. The absolute value of the calculated voltages ranges from 0.21 to 1.55 V vs Na/Na+; this is consistent with our experimental studies in our previous work,<sup>36</sup> where the equilibrium voltage for the conversion of Na<sub>4</sub>Ge<sub>4</sub> to Ge clathrate was observed at around 400 mV vs Na/Na+ at 300 °C (note that the DFT calculations assume a temperature of 0 K). The volume change of the clathrate during desodiation was also determined. As shown in Figure 2d, the decrease in volume between Na 24Ge 136 and Ge<sub>136</sub> after full desodiation is only 5.45%, which is much smaller compared to the other materials such as  $\alpha$ -NaSi (% $\nu$  = 230%),<sup>54</sup>  $\alpha$ -Na<sub>3</sub>Sb (% $\nu$  = 293-390%),<sup>55,56</sup> Na<sub>3</sub>P (% $\nu$  2 330%),<sup>57</sup> and  $Na_{3.75}Sn$  (%v = 420%)<sup>58</sup> investigated as Na reservoirs in Na-ion batteries. This small volume change between  $Na_{24}Ge_{136}$  and  $Ge_{136}$  could lead to good cycling stability. Overall, these calculations support the feasibility of desodiation of Na-filled Ge<sub>136</sub> clathrate to structures with variable Na content using electrochemical methods.

**3.3. Stability of the Hexagonal Na** $_{1-x}$ Ge $_{3+z}$  Phase. The hexagonal Na $_{1-x}$ Ge $_{3+z}$  phase, which we observed as an impurity to type II clathrates when the electrochemical oxidation reaction of Na $_4$ Ge $_4$  was performed at 300 °C, was the major product when the reaction was done at 350 °C. Rietveld refinement for this phase matched the structure reported in ref 59 (P6/m, no. 175), which can be described as an unusual zeolite-like framework consisting of covalently bonded Ge atoms that form large and small Na-filled channels (Figure 3a,b). Four of the Ge framework sites (denoted by Ge1, Ge2, Ge3, and Ge4) and one Na site (denoted as Na5) are fully occupied and make up the small channels. However, the Na6 and Ge7 sites in the large channels only have a partial

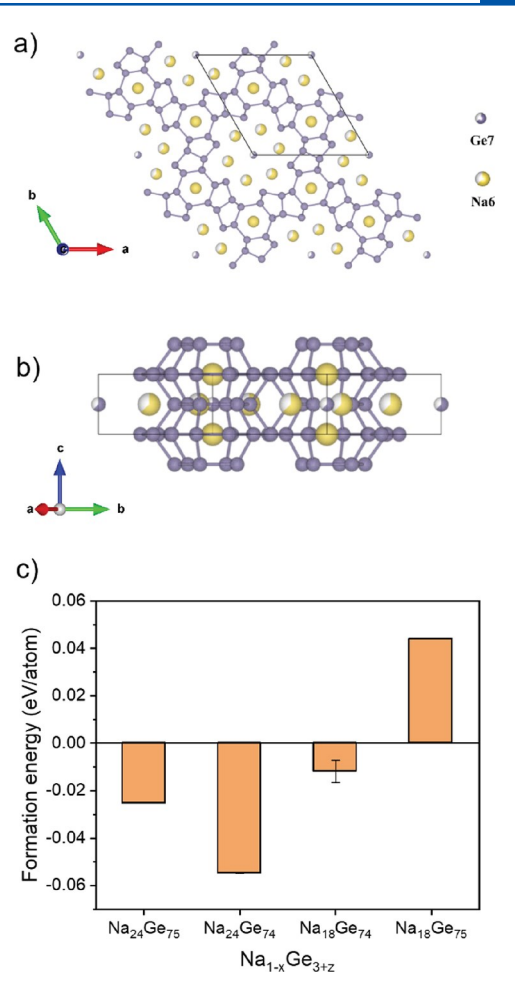


Figure 3. (a) Schematic of a  $2 \times 2 \times 1$  super cell for Na $_{1-x}$ Ge $_{3+z}$  when viewed along the c-axis with unit cell indicated with the diamond; (b) the unit cell of Na $_{1-x}$ Ge $_{3+z}$  viewed along the [120] axis. Na and Ge atoms are shown in yellow and purple, respectively. Partially filled yellow/purple atoms indicate the Na6/Ge7 sites with partial occupancy. (c) Formation energies for different compositions of Na $_{1-x}$ Ge $_{3+z}$  as calculated from the  $1 \times 1 \times 3$  supercell structures of Na $_{2}$ Ge $_{75}$ (all sites fully occupied), Na Ge (Na6 site fully occupied, the Ge7 site with occupancy of 2/3), Na Ge $_{18}$  (both Na6 and Ge7 sites with occupancy of 2/3), and Na Ge $_{18}$  (both Na6 site with occupancy of 2/3, the Ge7 site fully occupied). For Na Ge $_{31}$  and Na Ge $_{18}$ , several different configurations were considered for each composition and the formation energy in panel c is the average among them (see text, Tables S3 and S4 and Figures S2 and S3 for more details).

occupancy of 0.617, making the compound nonstoichiometric and described generally as  $Na_{1-x}Ge_{3+z}$ . It was observed that the occupancy of both Na6 and Ge7 sites can vary depending on the synthesis conditions. In particular, repeated grinding under a nitrogen atmosphere and then degassing (i.e., further heating the specimen under vacuum at 350 °C) were found to reduce the Na content.

To model the partial occupancies of the Na6 and Ge7 sites, a supercell model ( $1 \times 1 \times 3$ ) was used and the occupancy of 0.617 was treated to be approximately 0.667 (2/3). The supercell with each site fully occupied corresponds to a chemical composition of Na<sub>24</sub>Ge<sub>75</sub>, which has a calculated formation energy of -0.0254 eV/atom. To model the partial occupancy of the Ge7 site, one Ge atom out of the three equivalent positions in the supercell was removed, giving three

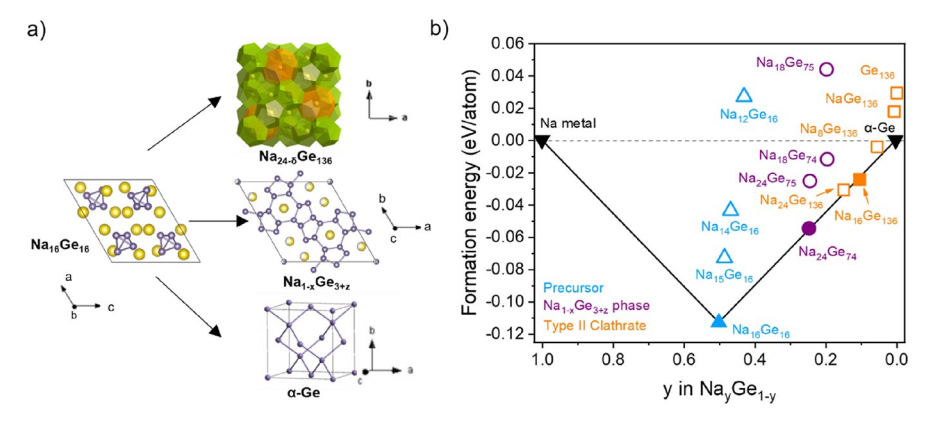


Figure 4. (a) Schematic showing the different products arising out of the electrochemical oxidation of the  $Na_{16}Ge_{16}$  precursor at different temperatures as reported in ref 36. (b) Calculated formation energies as a function of sodium content in  $Na_{16}Ge_{1-y}$  structures. The tie-line (black line) shows the convex hull obtained by joining together the globally stable structures. Phases on the tie-line are represented with solid symbols; phases above the hull are denoted using open symbols.

different geometrical configurations (Figure S2) with a composition of Na<sub>24</sub>Ge<sub>74</sub>. The formation energies of all three configurations are negative with negligible differences (Table S3), indicating they are energetically favorable. Since the configuration with Ge atoms removed from the third unit cell (configuration 3) had the lowest formation energy, this configuration was considered as the starting point to model the partial occupancy of the Na6 site. Because there are six equivalent positions for the Na6 site in the unit cell, the 1 × 1 × 3 supercell contains 18 of these sites. To model the partial occupancy of 2/3, 6 Na atoms need to be removed from the 18 equivalent Na6 sites to give a composition of Na<sub>18</sub>Ge<sub>74</sub>. There are many possible ways to remove those 6 Na atoms, and their geometrical configurations and formation energies are given in Figure S3 and Table S4. The average formation energy of all these possible configurations was calculated to be -0.012 eV/ atom. For the sake of completeness, we also modeled Na<sub>1-v</sub>Ge<sub>3+7</sub> with the Na6 site partially occupied but Ge7 site fully occupied (i.e., Na<sub>18</sub>Ge<sub>75</sub>) and obtained a formation energy of 0.044 eV/atom.

The results from the four  $Na_{1-x}Ge_{3+z}$  compositions studied (Figure 3c) show that the Na<sub>4</sub> Ge<sub>75</sub> and Na<sub>4</sub> Ge<sub>74</sub> structures in which the Na6 site is fully occupied are both favorable; however, the structure with partial occupancy of the Ge7 site is the more favorable of the two due to its more negative formation energy. This observation is consistent with the composition of Na<sub>1</sub>Ge<sub>3.25</sub> reported in materials synthesized from ref 59. Our results also show that the impurity phase with partial occupancy on both Na6 and Ge7 sites is feasible (Na<sub>18</sub>Ge<sub>74</sub>), which is again consistent with the compositions of  $\mathrm{Na_{0.71}Ge_{3.08}}$  and  $\mathrm{Na_{0.72}Ge_{3.13}}$  obtained from earlier studies. <sup>59,61</sup> Based on purely entropic considerations, we postulate that Na<sub>18</sub>Ge<sub>74</sub> could preferably form over Na<sub>24</sub>Ge<sub>75</sub> and Na<sub>24</sub>Ge<sub>74</sub> because the partial occupation on both Na6 and Ge7 sites would give rise to higher configurational entropy. To our knowledge, there have been no reports of the  $Na_{1-x}Ge_{3+z}$ phase with only the Na6 site partially occupied and the Ge7 site fully occupied (Na<sub>18</sub>Ge<sub>75</sub>). This can be explained by its positive formation energy of 0.044 eV/atom (Figure 3c). Thus, our approach of using a supercell model  $(1 \times 1 \times 3)$  to simulate the Na<sub>1-x</sub>Ge<sub>3+7</sub> phase is consistent and in good agreement with experimental results. Overall, these calculations demonstrate the different ways in which the Na<sub>1-x</sub>Ge<sub>3+z</sub> phase

can be modeled and highlight its preference for disorder in the structure.

3.4. Summary of Products Resulting from Electrochemical Oxidation of the Zintl Phase Precursor. Figure 4a highlights the different products obtained from the electrochemical oxidation of the Na Ge (Na Ge ) precursor at different temperatures, while Figure 4b shows the formation energies for the precursors and all the various product compositions studied herein. The tie-line (black line) shows the convex hull obtained by joining together the globally stable structures. Solid symbols represent phases on the tie-line, while those above the convex hull are denoted using open symbols. We see that  $Na_{16}Ge_{16'}$   $Na_{24}Ge_{74}$  ( $Na_{1-x}Ge_{3+z}$  with Na sites fully occupied and Ge7 site with 2/3 occupancy), and Na $Ge_{16}$   $_{136}$  (clathrate with Na atoms in the  $Ge_{20}$  cage centers) are found on the convex hull. Some of the compounds that are experimentally observed (Na-filled and nearly Na-free type II Ge clathrate) and Na<sub>1-x</sub>Ge<sub>2+7</sub> (with both Na7 and Ge6 sites with 2/3 occupancy) are only slightly above the hull, indicating that they are metastable compounds. This is evidenced by the fact that they decompose when heated to a certain temperature and do not reform when they cool down (420 °C for Ge 136 and  $\mathbb{Z}400$  °C for  $Na_{1-x}Ge_{3+z}^{60}$ ). This suggests that there could be some entropic contributions in these structures so that they become energetically favorable at high temperatures. Since the DFT-computed formation energies and convex hull diagram are performed at 0 K, the effects of entropy are not included.

3.5. Na Migration in the Zintl Phase Precursor. Since removal of Na from the Na Ge, precursor is required to form the various products shown in Figure 4, NEB calculations were performed to identify the mechanism for Na vacancy diffusion in the precursor structure. The NEB calculations were performed on the precursor structure with one Na vacancy (i.e., Na Ge 2the composition with the lowest formation energy among the investigated Na-deficient structures). In a unit cell of Na $_{15}$ Ge $_{16}$ , the Na vacancy density is fairly high at 6.25% (i.e., 1/16), so a 2  $\times$  2  $\times$  1 supercell with one Na vacancy ( $Na_{63}Ge_{64}$ ) was modeled, which corresponds to a vacancy density of 1.56% (i.e., 1/64). On the basis that Na vacancies at the 2a and 2b sites in  $Na_{15}Ge_{16}$  have the lowest formation energies (Figure 1d), vacancy diffusion in these sites was considered. Two migration pathways were studied: Path 1 involving Na vacancy migration from the 2a site to another 2a site, and Path 2 involving Na vacancy migration from a 2a site

to a 2b site. Figure 5a presents the calculated NEB energy barriers for both migration paths. The inserted schematics

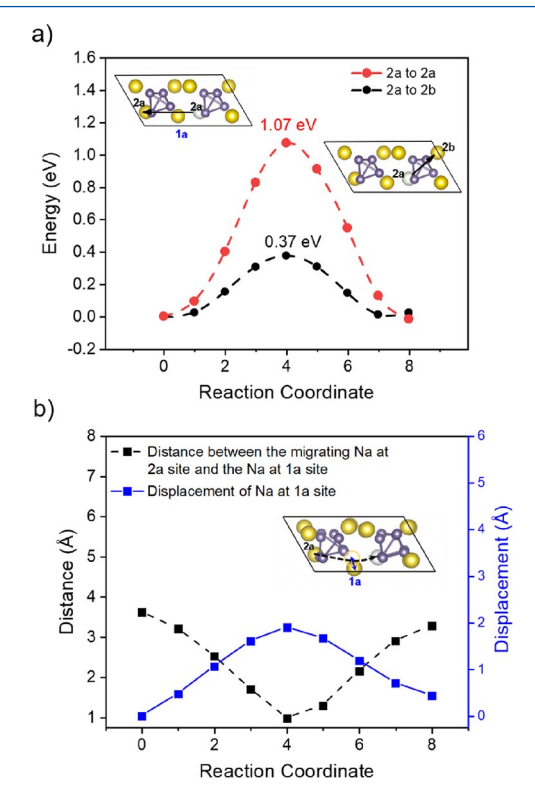


Figure 5. (a) NEB-calculated minimum energy paths for Na vacancy (white colored atom) migration from the 2a site to the 2a site (red) and from the 2a site to the 2b site (black), respectively, in  $\rm Nq_5\,Gq_{16}.$  Inset schematics show one-eighth of the supercell to illustrate the migration paths. (b) Inset structure snapshot shows the path for Na vacancy migration from the 2a site to the 2a site and the corresponding distance-displacement variation of the vacancy and the Na atom at the 1a site.

show only one-eighth of the supercell for clarity purposes. The energy barriers were found to be 1.07 eV for Path 1 and 0.37 eV for Path 2. Animations of these two migration paths can be found in Movies S1 and S2, respectively.

The reason for the large difference in the energy barrier between these two pathways can be understood upon inspection of Path 1 (Figure 5a inset, Movie S1), which reveals that the Na atom in the 1a site is positioned in the migration path and must be displaced to allow for the Na vacancy migration. From the inset snapshot in Figure 5b, it is clear that the Na atom at the 1a site blocks the migration path and experiences a large displacement when the migrating Na vacancy approaches. Initially, the distance between the migrating Na at the 2a site and the Na at the 1a site (shown by the black trace in Figure 5b) is 3.62 Å. This distance decreases and reaches a minimum of 0.98 Å at reaction coordinate 4. At this point, the Na atom at the 1a site experiences a large displacement of 1.89 Å from its initial position (shown in the blue trace in Figure 5b), which results in a high energy barrier for Path 1. On the other hand, for Path 2, there is no atom blocking the migrating pathway, which makes the energy barrier lower. These calculations suggest that Na vacancy (or atom) diffusion in the precursor prefers to follow Path 2 (i.e., 2a site to 2b site) rather than Path 1 (2a site to 2a site). The fairly low migration barrier 0.37 eV for Path 2

could explain why  $\mathrm{Na_4Ge_4}$  can be easily desodiated and serve as the precursor for the  $\mathrm{Na_{1-x}Ge_{3+z}}$  and Ge clathrate phases.

3.6. Na Migration in the Clathrate. 3.6.1. Na Migration through the Hexagonal Face in  $Na_1Ge_{136}$  and  $Na_{23}Ge_{136}$ Our experimental study<sup>36</sup> showed that the type II Ge clathrate synthesized from electrochemical oxidation of Na, Ge, can display variable Na content. To investigate the potential for type II Ge clathrates to be used as anodes for Na-ion batteries, the Na migration pathways within the structure should be considered. NEB calculations were reported for Li migration within type II Si clathrates 16,21 and in our preliminary study, 36 which found that migration of a Na atom through a shared hexagonal face between two adjacent Ge<sub>28</sub> cages (see the schematic inset in Figure 6a) in Na<sub>1</sub>Ge<sub>136</sub> had an energy barrier of 1.3 eV.36 Herein, to understand the effect of Na content of the Ge clathrate on the Na migration, NEB calculations were performed for a Na-rich clathrate,  $Na_{23}Ge_{136}$ , and compared to the clathrate containing a single Na atom. As shown in Figure 6a, the calculated minimum energy path for Na migration showed a higher barrier of 1.8 eV for Na<sub>23</sub>Ge<sub>136</sub> compared to 1.3 eV in Na<sub>1</sub>Ge<sub>136</sub>. Model schematics of both NEB pathways are shown in the inset of Figure 6a, with corresponding movies in Movies S3 and S4.

To understand the origins of the different Na migration energies in Na<sub>1</sub>Ge<sub>136</sub> and Na<sub>23</sub>Ge<sub>136</sub>, the transition states (i.e., reaction coordinate 4) were examined and compared. In both pathways, the transition state involves an area expansion of the hexagonal face of the Ge<sub>28</sub> cage as Na passes through to enter the connected  $Ge_{28}$  cage. The Ge-Ge bonds in the hexagonal face elongate from an initial distance of 2.51 Å to 22.67 Å in Na  $Ge_1$  and from 2.52 to 2.72 Å in  $Na_2Ge_{136}$ . This corresponding area expansion (as a percentage of the initial area) is 12.6% in  $\mathrm{Na_{1}Ge_{136}}$  and 16.6% in  $\mathrm{Na_{23}Ge_{136}}$  (Figure 6b). A larger area expansion is generally correlated to a greater distortion of the surrounding clathrate framework and results in a higher energy barrier.<sup>25</sup> In Na<sub>23</sub>Ge<sub>136</sub>, the migrating Na atom (shown as the red atom in Figure 6c) is surrounded by six other Na atoms (shown in yellow), which are located in the centers of the neighboring  $Ge_{20}$  cages (shaded in green in the inset of Figure 6a). When the migrating Na passes through the hexagonal face, the bond distance between the neighboring Na atoms (in the  $Ge_{20}$  cages) and the Ge atoms in the hexagon decreases from a Na-Ge distance of 23.60 Å to 3.49 Å at the transition state (Figure 6c), resulting in a higher energy barrier for Na migration.

3.6.2. Na Migration through the Pentagonal Face in  $Na_1Ge_{136}$  and  $Na_2Ge_{136}$ . The NEB-calculated energy barrier for Na migration between the  $Ge_{28}$  and  $Ge_{20}$  cages through a shared pentagonal face was reported to be  $4.0~{\rm eV}$  in  $Na_1Ge_{136}^{\phantom{1}.36}$ . Previous computational studies involving Li migration in type  $I^{16}$  and type  $I^{16}$  so clathrates have shown the possibility of another pathway, whereby temporary breakage of a Si-Si bond facilitates Li migration with a much lower energy barrier compared to Li migration through the center of the pentagonal face. This bond-breaking mechanism is possible with an additional Li atom present in an adjacent cage to help stabilize the transition state. To investigate whether this type of cooperative migration mechanism is also possible in Ge clathrates, the NEB calculations for Na migration from a  $Ge_{28}$  to  $Ge_{20}$  cage through a pentagonal face were performed with another Na atom inside an adjacent  $Ge_{28}$  cage in the Off Hex position. The energy profile for Na migration in this clathrate ( $Na_2Ge_{136}$ ) is compared to that for

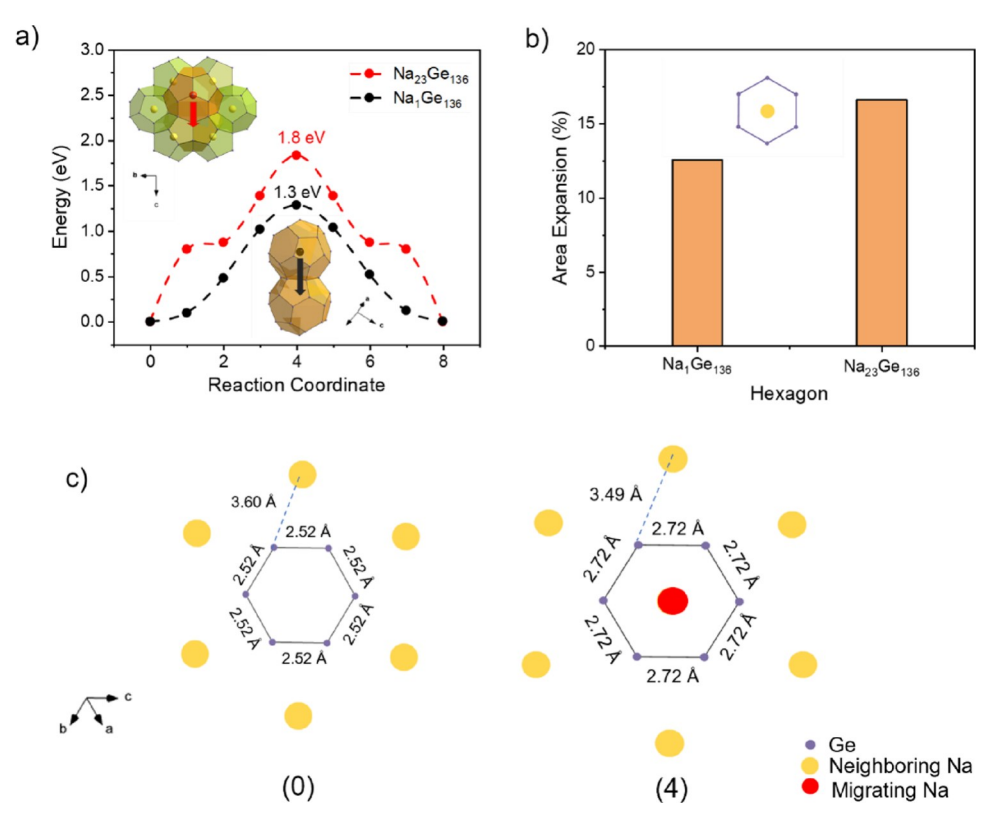


Figure 6. (a) NEB-calculated minimum energy paths for Na migration between two  $Ge_{28}$  cages (shaded orange in the inset schematics) through a shared hexagonal face in  $Na_{23}Ge_{136}$  (red) and  $Na_1Ge_{136}$  (black, data reproduced from ref 36) clathrate. (b) Area expansion of the hexagonal face in the clathrate at the transition state (reaction coordinate 4) relative to the initial area of the hexagon. (c) 2D schematic of the hexagonal face at the initial (0) and transition state (4) for Na migration in  $Na_{23}Ge_{136}$ .

the case without the neighboring Na atom ( $Na_1Ge_{136}$ ) in Figure 7a with movies of the migration pathways shown in Movies S5 and S6. The crystal schematics of the initial and transition state (reaction coordinates 0 and 4, respectively) are shown in Figure 7b.

We find that Na migration in  $Na_2Ge_{136}$  does not trigger the low-barrier, bond-breaking mechanism as seen in the Si clathrate case.<sup>21</sup> The migrating Na atom passes through the pentagon center with a slightly lower energy barrier of 3.85 eV when compared to that in  $\mathrm{Na_1Ge_{136}}$  without the adjacent  $\mathrm{Na}$ atom (Figure 7a). Figure 7c shows a comparison between  $Na_2Ge_{136}$  and  $Na_1Ge_{136}$  at the initial (0) and transition states (4). The pentagonal face in the transition state (4) displays an area expansion of 35% in Na<sub>2</sub>Ge<sub>136</sub> and 33% in Na<sub>1</sub>Ge<sub>136</sub> compared to the initial state. However, despite the larger area expansion, Na migration in  ${\rm Na_2Ge_{136}}$  shows a lower energy barrier. This is possibly because the neighboring Na atom (shown in yellow in Figure 7b,c) is only 3.30 Å away from the closest Ge atom in the initial state, which is comparable to the typical Na-Ge bond distance of 3.20–3.40 Å with Na at the Off hex position (see Table S5 for more details). We believe that this Na-Ge bond helps to facilitate the area expansion in Na<sub>2</sub>Ge<sub>136</sub> by elongating the Ge-Ge bond from 2.52 to 3.10 Å (shown as dark purple in Figure 7c) as the migrating Na atom reaches the pentagon center. Inspection of all the Ge-Ge bond lengths in the transition state of  $\mathrm{Na_2Ge_{136}}$  shows that this particular Ge-Ge bond is longer than the others in the pentagon; furthermore, the corresponding Ge-Ge bond in Na<sub>1</sub>Ge<sub>136</sub> is only 3.01 Å, as there is no such neighboring Na atom to facilitate the bond elongation. This suggests that the neighboring Na atom can still lower the Na migration barrier through the pentagonal face, although without the much lower energy barriers accompanied with bond breaking as seen in the Si clathrate case.<sup>21</sup> The implications and significance of neighboring Na atoms to the migration processes will be summarized in section 3.6.4.

3.6.3. Na Migration out of the  $Ge_{20}$  Cage. The barrier in Figure 7a (3.85 eV) is likely too high to facilitate Na diffusion through the Ge<sub>20</sub> cage, even given the synthesis temperatures of 300-400 °C. To investigate the energetics of Na migration out of a pentagonal face on the surface of the clathrate (rather than to a neighboring cage as in bulk diffusion), a slab model of the type II clathrate ( $Na_1Ge_{136}$ ) with a (001) surface was built with a thickness of 15.5 Å in the c-axis direction. Figure 8a shows the schematic of the Na migration path from the crosssection view (along the b-axis), while Figure 8b shows the plan view (viewing down the c-axis) (also shown in Movies S7-S8). Figure 8c presents the calculated NEB barrier for Na migration from the center of the  ${\rm Ge_{20}}$  cage to the outside of the surface through a pentagonal face. This pathway suggests a lower barrier of 1.22 eV compared to the above-mentioned situations. The detailed crystal structures of the initial (0), transition (4), and final (6) states of the Na migration in this slab model are shown in Figure 8d, which reveals a bondbreaking mechanism. Two of the Ge-Ge distances in the pentagonal face increase to 3.49 and 4.67 Å, in the transition state, which are much larger than the typical Ge-Ge bond lengths in the range of 2.49-2.58 Å seen in the initial and final

The results from the slab model calculations show that it is more energetically favorable for a Na atom to leave the small  $Ge_{20}$  cage if it is present at or near the surface of the clathrate

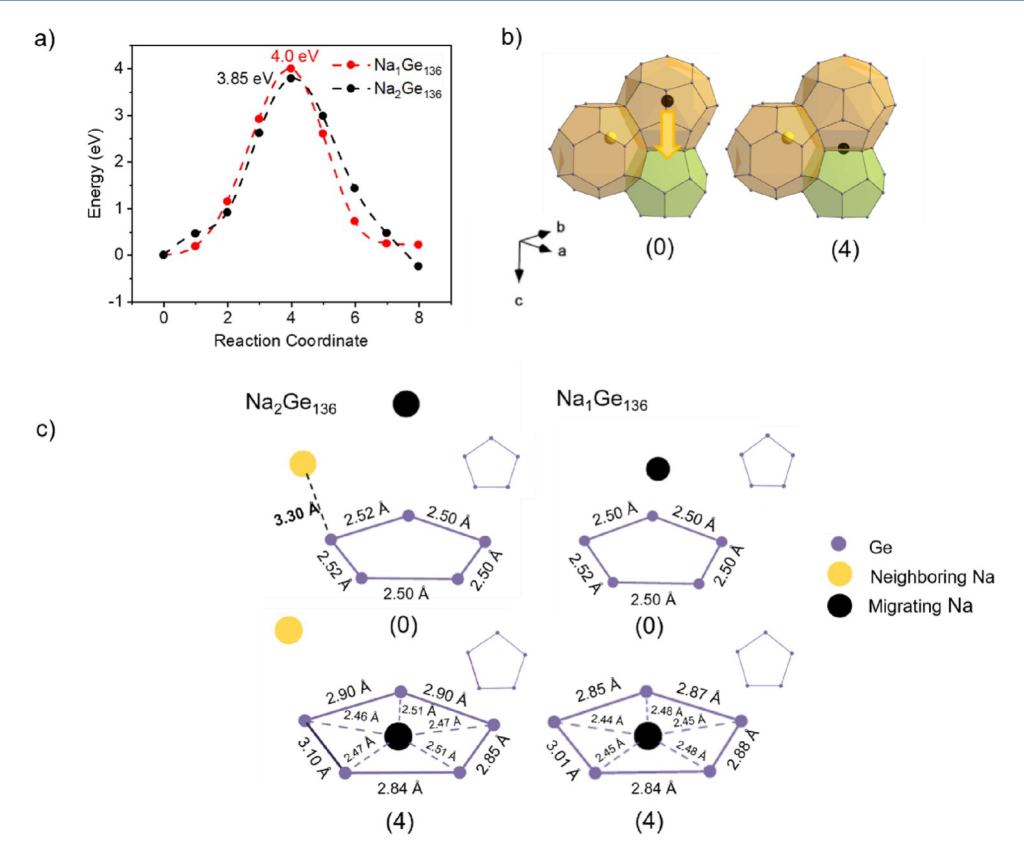


Figure 7. (a) NEB-calculated minimum energy paths for Na migration in  $Ge_{136}$  between a  $Ge_{28}$  and  $Ge_{20}$  cage through a shared pentagonal face in  $Na_1Ge_{136}$  (red), data reproduced from ref 36 and  $Na_2Ge_{136}$  (black). (b) Crystal models showing reaction coordinates 0 and 4 of the NEB path studied in  $Na_2Ge_{136}$ ; the  $Ge_{28}$  cage is shaded orange, the  $Ge_{20}$  cage is shaded green, the migrating Na atom is shown in black, the neighboring Na is shown in yellow, and the Ge atoms are in purple. (c) Schematic of the initial (0) and transition states (4) of  $Na_2Ge_{136}$  and  $Na_1Ge_{136}$  showing the shared pentagonal face formed by Ge atoms. The dark purple colored bond in (4) of  $Na_2Ge_{136}$  is the bond that is pulled by the neighboring Na atom (see text for details). The figures in the inset show the pentagonal face as viewed directly from the top.

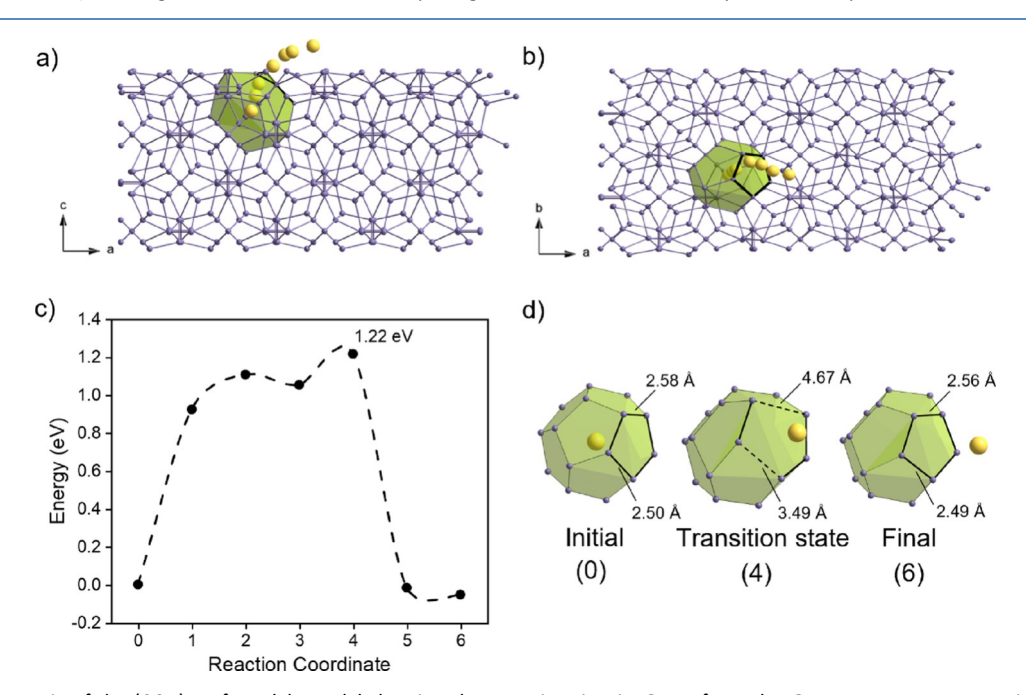


Figure 8. (a) Schematic of the (001) surface slab model showing the Na migration in  $Ge_{136}$  from the  $Ge_{20}$  cage center to outside of the clathrate structure when viewed along the *b*-axis. (b) The slab model viewed along the *c*-axis. (c) NEB-calculated minimum energy path for the migrating path shown in panel a. (d) Crystal models of the initial (0), transition (4), and final (6) state of Na migration in  $Ge_{136}$  showing the bond breaking mechanism. The two broken  $Ge_{136}$  bonds in the transition state (4) are denoted by the dashed lines with significantly increased bond distances (3.49 and 4.67 Å) compared to the values in the initial/final states.

ı

material. In addition to the slab model, we also considered the Na-rich structure Na<sub>23</sub>Ge<sub>136</sub> to see how Na migration through the Ge<sub>20</sub> cage was influenced by the presence of neighboring Na atoms (i.e., similar to the case of Na migration in Na 23 Ge 136 through the hexagonal face of the Ge<sub>28</sub> cage described in section 3.6.1). These calculations were performed using the PAW potentials in which Ge 3d and Na 2p electrons were included in the ion-core potentials, and only Ge 4s, 4p, and Na 3s electrons were explicitly treated as valence electrons. Such potential treatments still capture the essential valence electrons and thus are expected to predict reasonable results<sup>62,63</sup> while largely reducing the demand of computational resources. The details of the NEB barrier and pathway are provided in Figure S4 and Movie S9. A low energy barrier of 0.75 eV was obtained, and the migration path again involves a Ge-Ge bond breaking mechanism. This result showcases a possibility for facile Na migration through the Ge<sub>20</sub> cage and can help to explain the diffusion mechanism of Na evaporation (or thermal desodiation) from type II Ge clathrates during thermal treatment under vacuum.

3.6.4. Effect of Neighboring Na Atoms

Comparison between Na<sub>2</sub>Ge<sub>136</sub> and Na<sub>23</sub>Ge<sub>136</sub>. In the case of Na<sub>2</sub>Ge<sub>136</sub>, it was seen that the presence of one neighboring atom was able to reduce the barrier for Na migration through the pentagonal face from 4.0 to 3.85 eV (Figure 7a). However, in the case of Na<sub>23</sub>Ge<sub>136</sub>, despite the presence of 22 other Na atoms, Na migration through the hexagonal face showed a higher barrier of 1.8 eV as compared to 1.3 eV in Na<sub>1</sub>Ge<sub>136</sub> where there was no neighboring Na atom (Figure 6a). In summary, the presence of neighboring Na atoms helps to reduce the NEB barrier when Na migrates through the pentagonal face while showing the opposite effect when Na diffuses through the hexagonal face. This can be explained by examining the detailed structures of their transition states. For Na migration in Na<sub>2</sub>Ge<sub>136</sub>, the neighboring Na atom is able to preferentially elongate one particular Ge-Ge bond (from 2.52 to 3.10 Å in Figure 7c), thus aiding in opening/expanding the area of the pentagonal face to reduce the energy barrier. However, the elongation of these bonds is mitigated when Na atoms are present in the neighboring Ge<sub>20</sub> cages, causing all of the Ge-Ge bonds in the hexagon to elongate by a lesser degree (to only 2.72 Å in the transition state (Figure 6c). Therefore, Na migration in Na23Ge136 has a higher barrier than that in  $Na_1Ge_{13}6$ .

These results suggest that merely the presence of a neighboring Na atom in an adjacent cage does not necessarily help to reduce the barrier. This can be understood by examining the detailed cage structures in the clathrate. Considering Na migration between two large cages via a hexagonal face, the neighboring Na atoms are found in the adjacent  $Ge_{20}$  cages, as seen in  $Na_{23}Ge_{136}$ . These neighboring Na atoms occupy the center positions of the small cages, which are about 3.60 Å away from the hexagonal faces under consideration, therefore exhibiting limited influence on assisting Na migration through the hexagonal face. However, in Na migration between the large and small cages via a pentagonal face in Na2Ge136, the neighboring Na is located inside a large cage where Na has the potential to occupy three possible positions (Figure S1). In the lowest energy position, the Off hex position, the Na would only be found about 3.20-3.40 Å from the pentagonal face under consideration (Table S5), thus displaying reasonable influence in aiding the Na

migration through the pentagonal face to reduce the energy barrier.

We thereby propose two competing factors that can affect guest atom (Na) migration through the clathrate.

- First is the area expansion of the hexagonal/pentagonal face in the transition state as the guest atom (Na) passes through the face center. This expansion is due to the distortion of the framework atoms (Ge) as the migrating guest atom (Na) passes through the face and results in an increase in the energy barrier.
- Second is the presence of neighboring guest atoms? If favorable, it helps to stabilize the transition state by coordinating to the framework atoms and facilitating the expansion of the hexagonal/pentagonal face. This results in a decrease in the energy barrier.

To summarize the cases discussed above in sections 3.6.1 and 3.6.2, Na migration between two  ${\rm Ge_{28}}$  cages through a shared hexagonal face in  ${\rm Na_{23}Ge_{136}}$  is dominated by the first factor, resulting in an increase in the energy barrier. On the other hand, for Na migration in  ${\rm Na_{2}Ge_{136}}$  between a  ${\rm Ge_{28}}$  cage and  ${\rm Ge_{20}}$  cage through a shared pentagonal face, the effect of the second factor is more dominant than that of the first. Hence, this path shows a decrease in the energy barrier.

#### 4. CONCLUSIONS

First-principles DFT calculations were performed to understand the synthesis mechanism of type II Ge clathrates from the Zintl phase precursor  $Na_4Ge_4$ . It was found that it is energetically feasible for  $Na_4Ge_4$  to readily form Na vacancies, with the formation energy of the structure with Na vacancy densities of 6.25, 12.5, and 25% calculated to be -0.07, -0.05, and 0.03 eV/atom, respectively. The NEB calculations predicted a relatively low migration barrier of 0.37 eV for Na vacancy diffusion, which again verifies the ease at which desodiation of  $Na_4Ge_4$  can take place via electrochemical oxidation or thermal evaporation to synthesize type II Ge clathrates and  $Na_{1-x}Ge_{3+z}$ .

Na migration within the type II clathrate lattice was studied, and the effect of surrounding atoms on the migration pathway was understood. Energetically, Na prefers to occupy the Ge 20 cage center, followed by three more positions (coordinated off a hexagonal face, off a pentagonal face, or in the cage center, in that order) inside the large  $Ge_{28}$  cage. Na migration in the clathrate was found to be dominated by the pathway connecting the  $Ge_{28}$  cages via shared hexagonal faces. The energy barrier for this migration path is much lower (1.3 eV for Na<sub>1</sub>Ge<sub>136</sub>) than that of diffusing through a pentagonal face (4.0 eV for  $Na_1Ge_{136}$ ) connecting the  $Ge_{20}$  and  $Ge_{28}$  cages. The high energy barrier for Na migration through Ge 20 cages suggests that this pathway is kinetically restricted in the Nadilute regime. However, in the Na-rich regime (Na  $_{23}$ Ge  $_{136}$ ), an alternative pathway with a barrier of 0.75 eV was discovered via a Ge bond-breaking mechanism. Furthermore, a slab model showed a relatively low barrier of 1.22 eV for Na migration through a Ge<sub>20</sub> cage near the surface. This confirms that Na removal/evaporation from the clathrate is feasible, but only at higher temperatures (2300-400 °C as seen in our experiment) since the migration barriers are much higher than those that would enable significant room-temperature diffusion. The calculated voltages and small volume changes (25.5%) for Na removal from the clathrate indicate that Na intercalation of the empty clathrate Ge<sub>136</sub> is feasible and energetically favorable,

suggesting the type II germanium clathrates could be promising anode materials for Na-ion batteries.

The results presented here are informative for understanding the synthesis of clathrate materials via chemical deintercalation routes and may be helpful for the design of novel synthetic methods for these open framework materials. These insights also show that first-principles DFT methods can be an effective method in guiding researchers in the design and evaluation of new clathrate compounds as viable materials for energy storage applications.

# ?

#### **ASSOCIATED CONTENT**

#### Supporting Information

The Supporting Information is available free of charge at https://pubs.acs.org/doi/10.1021/acs.jpcc.3c02343.

NEB pathway for Na vacancy diffusion from the 2a site to the 2a site in  $Na_4Ge_4$  (AVI)

NEB pathway for Na vacancy diffusion from the 2a site to the 2b site in  $Na_4Ge_4$  (AVI)

NEB pathway for Na migration between two  $Ge_{28}$  cages through a shared hexagonal face in NaGe<sub>136</sub> (AVI)

NEB pathway for Na migration between two  $Ge_{28}$  cages in  $Na_{23}Ge_{136}$  through a shared hexagonal face (AVI)

NEB pathway for Na migration between a  $\rm Ge_{28}$  and  $\rm Ge_{20}$  cage through a shared pentagonal face in NaGe $_{136}$  (AVI) NEB pathway for Na migration between a  $\rm Ge_{28}$  and  $\rm Ge_{20}$  cage through a shared pentagonal face in Na $_2$ Ge $_{136}$  (AVI)

NEB pathway for Na migration from a  $Ge_{20}$  cage in  $Na_1Ge_{136}$  slab model to outside the clathrate structure via a bond-breaking mechanism, along the b-axis (AVI) NEB pathway for Na migration from a  $Ge_{20}$  cage in  $Na_1Ge_{136}$  slab model to outside the clathrate structure via a bond-breaking mechanism, along the c-axis (AVI) NEB pathway for Na migration between a  $Ge_{20}$  cage and a  $Ge_{28}$  cage through a shared pentagonal face in  $Na_{23}Ge_{136}$  via a bond-breaking mechanism (AVI)

Na-filled type II germanium clathrate (Na<sub>24</sub>Ge<sub>136</sub>) structure (CIF)

 $Na_{1-x}Ge_{3+z}$  structure (CIF)

Na<sub>4</sub>Ge<sub>4</sub> structure (CIF)

Calculated total and formation energies for the Zintl phase precursor structure with two and four Na vacancies, calculated energies and structures for  $Na_{1-x}Ge_{3+z}$  with the Ge7 site treated with partial occupancy of 2/3 or with both Na6 and Ge7 sites treated with partial occupancy of 2/3, calculated Na-Ge distances and schematic for Na at different sites in  $Ge_{28}$ , and NEB minimum energy path and crystal model schematics for Na migration in  $Na_{23}Ge_{136}$  through a shared pentagonal face via the bond-breaking mechanism (PDF)

# AUTHOR INFORMATION Corresponding Authors

Xihong Peng – College of Integrative Sciences and Arts, Arizona State University Polytechnic Campus, Mesa, Arizona 85212, United States; Email: xihong.peng@asu.edu

Candace K. Chan – Materials Science and Engineering, School for Engineering of Matter, Transport and Energy, Arizona State University, Tempe, Arizona 85827, United States; orcid.org/0000-0003-4329-4865; Email: candace.chan@asu.edu

#### Author

Anirudh Nandakumar – Materials Science and Engineering, School for Engineering of Matter, Transport and Energy, Arizona State University, Tempe, Arizona 85827, United States; orcid.org/0009-0002-4285-3960

Complete contact information is available at: https://pubs.acs.org/10.1021/acs.jpcc.3c02343

#### **Notes**

The authors declare no competing financial interest.

## ? ACKNOWLEDGMENTS

This work was supported by funding from NSF DMR 1710017 and DMR 2004514. The authors acknowledge Research Computing at Arizona State University for providing computational resources that contributed to the research results reported within this paper.

### REFERENCES

- (1) Hubner, J.-M.; Prots, Y.; Schnelle, W.; Bobnar, M.; König, M.; Baitinger, M.; Simon, P.; Carrillo-Cabrera, W.; Ormeci, A.; Svanidze, E.; Grin, Y.; Schwarz, U. In-Cage Interactions in the Clathrate Superconductor Sr<sub>8</sub>Si<sub>46</sub>: *Chemistry* 2020, *26*, 830–838.
- (2) Bryan, J. D.; Srdanov, V. I.; Stucky, G. D.; Schmidt, D. Superconductivity in Germanium Clathrate Ba<sub>8</sub> Ga<sub>16</sub> Ge<sub>30</sub>. *Phys. Rev. B* 1999, *60*, 3064–3067.
- (3) Connétable, D.; Timoshevskii, V.; Masenelli, B.; Beille, J.; Marcus, J.; Barbara, B.; Saitta, A. M.; Rignanese, G.-M.; Mélinon, P.; Yamanaka, S.; Blase, X. Superconductivity in Doped sp<sup>3</sup> Semiconductors: The Case of the Clathrates. *Phys. Rev. Lett.* 2003, *91*, No. 247001.
- (4) Kawaguchi, T.; Tanigaki, K.; Yasukawa, M. Ferromagnetism in Germanium Clathrate: Ba<sub>8</sub>Mn<sub>2</sub>Ge<sub>44</sub>. *Appl. Phys. Lett.* 2000, 77, 3438–3440
- (5) Böhme, B.; Minella, C. B.; Thoss, F.; Lindemann, I.; Rosenburg, M.; Pistidda, C.; Møller, K. T.; Jensen, T. R.; Giebeler, L.; Baitinger, M.; Gutfleisch, O.; Ehrenberg, H.; Eckert, J.; Grin, Y.; Schultz, L. B1-Mobilstor: Materials for Sustainable Energy Storage Techniques Lithium Containing Compounds for Hydrogen and Electrochemical Energy Storage. *Adv. Eng. Mater.* 2014, *16*, 1189–1195.
- (6) Neiner, D.; Okamoto, N. L.; Condron, C. L.; Ramasse, Q. M.; Yu, P.; Browning, N. D.; Kauzlarich, S. M. Hydrogen Encapsulation in a Silicon Clathrate Type I Structure: Na<sub>5.5</sub>(H<sub>2</sub>)<sub>2.15</sub>Si<sub>46</sub>: Synthesis and Characterization. *J. Am. Chem. Soc.* 2007, *129*, 13857–13862.
- (7) Neiner, D.; Okamoto, N. L.; Yu, P.; Leonard, S.; Condron, C. L.; Toney, M. F.; Ramasse, Q. M.; Browning, N. D.; Kauzlarich, S. M. Synthesis and Characterization of K<sub>8-x</sub>(H<sub>2</sub>)YSi<sub>46</sub>. *Inorg. Chem.* 2010, 49, 815–822.
- (8) Baranowski, L. L.; Krishna, L.; Martinez, A. D.; Raharjo, T.; Stevanovic, V.; Tamboli, A. C.; Toberer, E. S. Synthesis and Optical Band Gaps of Alloyed Si–Ge Type II Clathrates. *J. Mater. Chem. C* 2014, *2*, 3231–3237.
- (9) Martinez, A. D.; Krishna, L.; Baranowski, L. L.; Lusk, M. T.; Toberer, E. S.; Tamboli, A. C. Synthesis of Group IV Clathrates for Photovoltaics. *IEEE J. Photovoltaics* 2013, *3*, 1305–1310.
- (10) Kume, T.; Ohashi, F.; Sakai, K.; Fukuyama, A.; Imai, M.; Udono, H.; Ban, T.; Habuchi, H.; Suzuki, H.; Ikari, T.; Sasaki, S.; Nonomura, S. Thin Film of Guest-Free Type-II Silicon Clathrate on Si(111) Wafer. *Thin Solid Films* 2016, 609, 30–34.
- (11) Dolyniuk, J.-A.; Owens-Baird, B.; Wang, J.; Zaikina, J. V.; Kovnir, K. Clathrate Thermoelectrics. *Mater. Sci. Eng., R* 2016, *108*, 1–46.
- (12) Christensen, M.; Johnsen, S.; Iversen, B. B. Thermoelectric Clathrates of Type I. *Dalton Trans.* 2010, *39*, 978–992.

- (13) Candolfi, C.; Aydemir, U.; Baitinger, M.; Oeschler, N.; Steglich, F.; Grin, Y. Thermoelectric Properties of the Clathrate I Ba<sub>8</sub>Ge<sub>43</sub> <sub>3</sub>. *J. Electron. Mater.* 2010, *39*, 2039–2042.
- (14) Baitinger, M.; Böhme, B.; Wagner, F. R.; Schwarz, U. Zintl Defects in Intermetallic Clathrates. *Z. Anorg. Allg. Chem.* 2020, *646*, 1034–1041.
- (15) Langer, T.; Dupke, S.; Trill, H.; Passerini, S.; Eckert, H.; Pöttgen, R.; Winter, M. Electrochemical Lithiation of Silicon Clathrate-II. *J. Electrochem. Soc.* 2012, *159*, A1318–A1322.
- (16) Yang, J.; Tse, J. S. Silicon Clathrates as Anode Materials for Lithium Ion Batteries? *J. Mater. Chem. A* 2013, 1, 7782–7789.
- (17) Wagner, N. A.; Raghavan, R.; Zhao, R.; Wei, Q.; Peng, X.; Chan, C. K. Electrochemical Cycling of Sodium-Filled Silicon Clathrate. *ChemElectroChem* 2014, 1, 347–353.
- (18) Li, Y.; Raghavan, R.; Wagner, N. A.; Davidowski, S. K.; Baggetto, L.; Zhao, R.; Cheng, Q.; Yarger, J. L.; Veith, G. M.; Ellis-Terrell, C.; Miller, M. A.; Chan, K. S.; Chan, C. K. Type I Clathrates as Novel Silicon Anodes: An Electrochemical and Structural Investigation. *Adv. Sci.* 2015, *2*, No. 1500057.
- (19) Zhao, R.; Bobev, S.; Krishna, L.; Yang, T.; Weller, J. M.; Jing, H.; Chan, C. K. Anodes for Lithium-Ion Batteries Based on Type I Silicon Clathrate Ba<sub>8</sub>Al<sub>16</sub>Si<sub>30</sub> Role of Processing on Surface Properties and Electrochemical Behavior. *ACS Appl. Mater. Interfaces* 2017, *9*, 41246–41257.
- (20) Dopilka, A.; Childs, A.; Bobev, S.; Chan, C. K. Solid-State Electrochemical Synthesis of Silicon Clathrates Using a Sodium-Sulfur Battery Inspired Approach. *J. Electrochem. Soc.* 2021, *168*, No. 020516.
- (21) Dopilka, A.; Weller, J. M.; Ovchinnikov, A.; Childs, A.; Bobev, S.; Peng, X.; Chan, C. K. Structural Origin of Reversible Li Insertion in Guest-Free, Type-II Silicon Clathrates. *Adv. Energy Sustainability Res.* 2021, *2*, No. 2000114.
- (22) Dopilka, A.; Zhao, R.; Weller, J. M.; Bobev, S.; Peng, X.; Chan, C. K. Experimental and Computational Study of the Lithiation of Ba Al &Ge<sub>Y</sub> 46-yBased Type I Germanium Clathrates. *ACS Appl. Mater. Interfaces* 2018, *10*, 37981–37993.
- (23) Dopilka, A.; Childs, A.; Ovchinnikov, A.; Zhao, R.; Bobev, S.; Peng, X.; Chan, C. K. Structural and Electrochemical Properties of Type VIII BasGa<sub>16- $\delta$ </sub>Sn<sub>30+ $\delta$ </sub>Clathrate ( $\delta$  $\approx$  1) during Lithiation. *ACS Appl. Mater. Interfaces* 2021, 42564.
- (24) Peng, X.; Wei, Q.; Li, Y.; Chan, C. K. First-Principles Study of Lithiation of Type I Ba-Doped Silicon Clathrates. *J. Phys. Chem. C* 2015, *119*, 28247–28257.
- (25) Dopilka, A.; Peng, X.; Chan, C. K. Ab Initio Investigation of Li and Na Migration in Guest-Free, Type I Clathrates. *J. Phys. Chem. C* 2019, *123*, 22812–22822.
- (26) Arrieta, U.; Katcho, N. A.; Arcelus, O.; Carrasco, J. First-Principles Study of Sodium Intercalation in Crystalline Na $\times$ Si24 (0  $\leq$  x  $\leq$  4) as Anode Material for Na-Ion Batteries. *Sci. Rep.* 2017, 7, 5350.
- (27) Urban, A.; Seo, D.-H.; Ceder, G. Computational Understanding of Li-Ion Batteries. *npj Comput. Mater.* 2016, *2*, 16002.
- (28) Mayo, M.; Griffith, K. J.; Pickard, C. J.; Morris, A. J. Ab Initio Study of Phosphorus Anodes for Lithium- and Sodium-Ion Batteries. *Chem. Mater.* 2016, *28*, 2011–2021.
- (29) He, Q.; Yu, B.; Li, Z.; Zhao, Y. Density Functional Theory for Battery Materials. *Energy Environ. Mater.* 2019, *2*, 264–279.
- (30) Kumar, R.; Hazama, Y.; Ohashi, F.; Jha, H. S.; Kume, T. A Fabrication Method for Type-II Ge Clathrate Film by Annealing of Ge Film Covered with Na Layer. *Thin Solid Films* 2021, *734*, No. 138859.
- (31) Kumar, R.; Maeda, T.; Hazama, Y.; Ohashi, F.; Jha, H. S.; Kume, T. Growth of Ge Clathrate on Sapphire and Optical Properties. *Jpn. J. Appl. Phys.* 2020, 59.
- (32) Kumar, R.; Yamada, K.; Ohashi, F.; Jha, H. S.; Kume, T. Optimization of Synthesis Condition of Type II Ge Clathrate Film. *Jpn. J. Appl. Phys.* 2023, *62*, SD1020.
- (33) Kasper, J. S.; Hagenmuller, P.; Pouchard, M.; Cros, C. Clathrate Structure of Silicon Na $^8$ Si $^{46}$  and Na $^x$ Si $^{136}$  (x < 11). *Science* 1965, *150*, 1713–1714.

- (34) Krishna, L.; Baranowski, L. L.; Martinez, A. D.; Koh, C. A.; Taylor, P. C.; Tamboli, A. C.; Toberer, E. S. Efficient Route to Phase Selective Synthesis of Type II Silicon Clathrates with Low Sodium Occupancy. *CrystEngComm* 2014, *16*, 3940–3949.
- (35) Beekman, M.; Nolas, G. S. Synthesis and Thermal Conductivity of Type II Silicon Clathrates. *Phys. B* 2006, *383*, 111–114.
- (36) Dopilka, A.; Ovchinnikov, A.; Childs, A.; Bobev, S.; Peng, X.; Chan, C. K. Synthesis of Type II Ge and Ge-Si Alloyed Clathrates Using Solid-State Electrochemical Oxidation of Zintl Phase Precursors. *Inorg. Chem.* 2022, *61*, 12363–12372.
- (37) Guloy, A. M.; Tang, Z.; Ramlau, R.; Böhme, B.; Baitinger, M.; Grin, Y. Synthesis of the Clathrate-II  $K_{8.6}(_4)Ge_{136}$  by Oxidation of  $K_4Ge_9$  in an Ionic Liquid. *Eur. J. Inorg. Chem.* 2009, *6*, 2455–2458.
- (38) Böhme, B.; Hoffmann, S.; Baitinger, M.; Grin, Y. Application of N-Dodecyltrimethylammonium Chloride for the Oxidation of Intermetallic Phases. *Z. Naturforsch., B: J. Chem. Sci.* 2011, *66*, 230–238.
- (39) Feng, X. J.; Lerch, S.; Biller, H.; Micksch, M.; Schmidt, M.; Baitinger, M.; Strassner, T.; Grin, Y.; Böhme, B. Reactivity and Controlled Redox Reactions of Salt-like Intermetallic Compounds in Imidazolium-Based Ionic Liquids. *ChemistryOpen* 2021, 10, 205–215.
- (40) Carrillo-Cabrera, W.; Cardoso Gil, R.; Somer, M.; Persil, O.; Von Schnering, H.  $Na_{12}Ge_{17}$ : A Compound with the Zintl Anions  $[Ge_4]^{4-}$  and  $[Ge_9]^{4-}$  Synthesis, Crystal Structure, and Raman Spectrum. *Z. Anorg. Allg. Chem.* 2003, *629*, 601–608.
- (41) Böhme, B. An Electrochemical Approach toward the Metastable Type II Clathrate Germanium Allotrope. *Inorg. Chem.* 2020, *59*, 11920–11924.
- (42) Kresse, G.; Furthmuller, J. Efficient Iterative Schemes for Ab Initio Total-Energy Calculations Using a Plane-Wave Basis Set. *Phys. Rev. B* 1996, *54*, 11169–11186.
- (43) Kresse, G.; Joubert, D. From Ultrasoft Pseudopotentials to the Projector Augmented-Wave Method. *Phys. Rev. B* 1999, *59*, 1758–1775.
- (44) Perdew, J. P.; Burke, K.; Ernzerhof, M. Generalized Gradient Approximation Made Simple. *Phys. Rev. Lett.* 1996, *77*, 3865–3868.
- (45) Aydinol, M. K.; Kohan, A. F.; Ceder, G.; Cho, K.; Joannopoulos, J. Ab Initio Study of Lithium Intercalation in Metal Oxides and Metal Dichalcogenides. *Phys. Rev. B.* 1997, *56*, 1354.
- (46) Henkelman, G.; Uberuaga, B. P.; Jónsson, H. A Climbing Image Nudged Elastic Band Method for Finding Saddle Points and Minimum Energy Paths Graeme. *J. Chem. Phys.* 2006, *113*, 9901.
- (47) Momma, K.; Izumi, F. VESTA 3 for Three-Dimensional Visualization of Crystal, Volumetric and Morphology Data. *J. Appl. Crystallogr.* 2011, 44, 1272–1276.
- (48) Brandenburg, K. Diamond: Crystal and Molecular Structure Visualization; DIAMOND Crystal Impact GbR: Bonn, Germany, 2006.
- (49) Herráez, A.; Hanson, R. M.; Glasser, L. Jmol: An Open-Source Java Viewer for Chemical Structures in 3D. *Angel. Biochem. Mol. Biol. Educ.* 2009, 8.
- (50) Morito, H.; Momma, K.; Yamane, H. Crystal Structure Analysis of Na<sup>4</sup>Si<sup>4</sup>\*Ge<sup>x</sup> by Single Crystal X-Ray Diffraction. *J. Alloys Compd.* 2015, *623*, 473–479.
- (51) Slingsby, J. G.; Rorrer, N. A.; Krishna, L.; Toberer, E. S.; Koh, C. A.; Maupin, C. M. Dynamic Free Energy Surfaces for Sodium Diffusion in Type II Silicon Clathrates. *Phys. Chem. Chem. Phys.* 2016, *18*, 5121–5128.
- (52) Feng, X. J.; Bobnar, M.; Lerch, S.; Biller, H.; Schmidt, M.; Baitinger, M.; Strassner, T.; Grin, Y.; Böhme, B. Type-II Clathrate  $Na^{24-\delta}Ge^{136}$  from a Redox-Preparation Route. *Chem. Eur. J.* 2021, *27*, 12776–12787.
- (53) Guloy, A. M.; Ramlau, R.; Tang, Z.; Schnelle, W.; Baitinger, M.; Grin, Y. A Guest-Free Germanium Clathrate. *Nature* 2006, *443*, 320–323.
- (54) Chou, C. Y.; Lee, M.; Hwang, G. S. A Comparative First-Principles Study on Sodiation of Silicon, Germanium, and Tin for Sodium-Ion Batteries. *J. Phys. Chem. C* 2015, *119*, 14843–14850.

- (55) Baggetto, L.; Ganesh, P.; Sun, C. N.; Meisner, R. A.; Zawodzinski, T. A.; Veith, G. M. Intrinsic Thermodynamic and Kinetic Properties of Sb Electrodes for Li-Ion and Na-Ion Batteries: Experiment and Theory. *J. Mater. Chem. A* 2013, *1*, 7985–7994.
- (56) Qian, J.; Chen, Y.; Wu, L.; Cao, Y.; Ai, X.; Yang, H. High Capacity Na-Storage and Superior Cyclability of Nanocomposite Sb/C Anode for Na-Ion Batteries. *Chem. Commun.* 2012, 48, 7070–7072.
- (57) Liu, Y.; Liu, Q.; Jian, C.; Cui, D.; Chen, M.; Li, Z.; Li, T.; Nilges, T.; He, K.; Jia, Z.; Zhou, C. Red-Phosphorus-Impregnated Carbon Nanofibers for Sodium-Ion Batteries and Liquefaction of Red Phosphorus. *Nat. Commun.* 2020, *11*, 2520.
- (58) Wang, J. W.; Liu, X. H.; Mao, S. X.; Huang, J. Y. Microstructural Evolution of Tin Nanoparticles during in Situ Sodium Insertion and Extraction. *Nano Lett.* 2012, *12*, 5897–5902.
- (59) Beekman, M.; Stefanoski, S.; Wong-Ng, W.; Kaduk, J. A.; Huang, Q.; Reeg, C.; Bowers, C. R.; Nolas, G. S. Structure and Thermal Conductivity of Na<sub>1-x</sub>Ge<sub>3+z</sub>. *J. Solid State Chem.* 2010, *183*, 1272–1277.
- (60) Beekman, M.; Kaduk, J. A.; Huang, Q.; Wong-Ng, W.; Yang, Z.; Wang, D.; Nolas, G. S. Synthesis and Crystal Structure of Na<sub>1-x</sub> Ge<sub>3+2</sub>: A Novel Zeolite-like Framework Phase in the Na–Ge System. *Chem. Commun.* 2007, *8*, 837–839.
- (61) Jakobsen, H. J.; Bildsøe, H.; Beekman, M.; Stefanoski, S.; Nolas, G. S.; Bowers, C. R. Low-Temperature <sup>23</sup>Na MAS NMR Reveals Dynamic Effects and Compositions for the Large and Small Channels in the Zeolite-like Ge-Framework of Na<sub>1-x</sub>Ge<sub>3+z</sub> Materials. *J. Phys. Chem. C* 2014, *118*, 28890–28897.
- (62) Spiewak, P.; Sueoka, K.; Vanhellemont, J.; Kurzydłowski, K. J.; Młynarczyk, K.; Wabinski, P.; Romandic, I. Ab Initio Calculation of the Formation Energy of Charged Vacancies in Germanium. *Phys. B* 2007, 401-402, 205–209.
- (63) Ansari, J. N.; Sauer, K. L.; Glasbrenner, J. K. The Predictive Power of Different Projector-Augmentedwave Potentials for Nuclear Quadrupole Resonance. *Crystals* 2019, *9*, 507.